Probing the effects of dextran-coated CeO₂ nanoparticles on lung fibroblasts using multivariate single-cell Raman spectroscopy

Mirjana Mićević, Sonja Čalija, Lela Korićanac, Jelena Žakula, Aleksandra Vilotić, Marko Radović, Igor Golić, Aleksandra Korać, Mirjana Nacka-Aleksić, Bojan Stojadinović & Zorana Dohčević-Mitrović

Taylor & Francis
Taylor & Francis Group

RESEARCH ARTICLE

OPEN ACCESS   Check for updates

Probing the effects of dextran-coated CeO$_2$ nanoparticles on lung fibroblasts using multivariate single-cell Raman spectroscopy

Mirjana Mićević[a], Sonja Čalija[a], Lela Korićanac[b], Jelena Žakula[b], Aleksandra Vilotić[c], Marko Radović[d], Igor Golić[e], Aleksandra Korać[e], Mirjana Nacka-Aleksić[c], Bojan Stojadinović[a] and Zorana Dohčević-Mitrović[a]

[a]Institute of Physics Belgrade, University of Belgrade, Belgrade, Serbia; [b]Vinča Institute of Nuclear Sciences, National Institute of the Republic of Serbia, University of Belgrade, Belgrade, Serbia; [c]Institute for the Application of Nuclear Energy, Department for Biology of Reproduction, University of Belgrade, Belgrade, Serbia; [d]BioSense Institute, University of Novi Sad, Novi Sad, Serbia; [e]Center for Electron Microscopy, Faculty of Biology, University of Belgrade, Belgrade, Serbia

ABSTRACT

In this study, we investigated the cytotoxic effect of highly soluble dextran-coated CeO$_2$ nanoparticles on human fetal lung fibroblasts MRC-5. We examined individual nanoparticle-treated cells by Raman spectroscopy and analyzed Raman spectra using non-negative principal component analysis and k-means clustering. In this way, we determined dose-dependent differences between treated cells, which were reflected through the intensity change of lipid, phospholipid and RNA-related Raman modes. Performing standard biological tests for cell growth, viability and induction of apoptosis in parallel, these changes were correlated with nanoparticle-induced apoptotic processes. The cells with specific spectral characteristics, referring to non-apoptotic, but possibly autophagic cell death modality, were also detected. Additionally, Raman imaging combined with principal component and vertex component analysis was used to map the spatial distribution of biological molecules in treated and untreated cells. This work provided the description of different resulting states of the treated cells depending on the dextran-coated CeO$_2$ nanoparticles dose, which can be later used in the design of the nanoparticles for industrial or medical applications. The wide content of information resulting from single-cell Raman spectroscopy has the potential to detect biochemical changes caused by nanoparticles that would otherwise require a series of expensive and time-consuming standard biological techniques.

1. Introduction

Cerium oxide (CeO$_2$) is a rare earth metal oxide, characterized by a fluorite cristal structure with a significant concentration of oxygen vacancies (Campbell and Peden 2005). Cerium can exist in two oxidation forms, Ce^{3+} and Ce^{4+} (Reed et al. 2014). By receiving or releasing one or more oxygen atoms from crystal lattice and changing the Ce^{3+}/Ce^{4+} ratio at the same time, cerium oxide can easily cycle between CeO$_2$ and CeO$_{2-x}$ states. Such characteristics provide CeO$_2$ with excellent redox and catalytic capabilities, used for industrial application (Ma et al. 2018), but also crucial for biological activities. Namely, CeO$_2$ nanoparticles (NPs) can mimic the activity of numerous cellular enzymes, like

superoxide dismutase and catalase, but also oxidase and peroxidase (Walkey et al. 2015; Feng et al. 2022). This means that those NPs can act both as scavenger and generator of harmful reactive oxygen species (ROS) in the cell. The imbalance between the pro-oxidant and anti-oxidant activities of CeO$_2$ can lead to oxidative stress, resulting in apoptotic cell death, which is considered the main reason for the possible cytotoxicity of these NPs (Jana et al. 2014; Mittal and Pandey 2014; Nourmohammadi et al. 2019).

Nowadays, CeO$_2$ NPs are present in a large number of industrial products, such as fuel catalysts, polishing agents, gas sensors etc. (Reed et al. 2014; Zhou et al. 2021; Jung, Kittelson, and Zachariah 2005; Mangalaraja et al. 2010). Emitted into the air

from such sources, they can be inhaled and potentially affect the lungs and other internal organs. The toxicity of inhaled CeO_2 NPs, manifested by decreased viability of lung cells and induction of inflammation, has been demonstrated in some *in vivo* studies in rat and mouse model systems (Srinivas et al. 2011; Guo et al. 2019). It has also been shown that these NPs can cause pulmonary fibrosis, a very serious and progressive disease with fatal outcome (Annangi et al. 2021; Hill et al. 2019). Contrary to these studies, other *in vivo* and *in vitro* experiments showed that CeO_2 NPs can protect cells from the negative influence of free radicals, such as those from cigarette smoke (Niu, Wang, and Kolattukudy 2011; Chen et al. 2006). There is limited information about the mechanisms of CeO_2 NPs interactions with different bronchiolar and alveolar cell types and their interplay during lung tissue remodeling (Annangi et al. 2021; Ma et al. 2012).

MRC-5 is a cell line derived from human fetal lung fibroblasts, connective tissue cells that play a key role in the development of pulmonary fibrosis (Ortiz-Zapater et al. 2022). In the literature, only few data about the possible cytotoxic effect of CeO_2 NPs on these cells are available and the results of the performed studies are not clear and consistent, evidencing both weak and strong cytotoxicity (Pešić et al. 2015; Spezzati et al. 2017; Alghamdi 2023). Some studies have shown that the cytotoxic effect is highly dependent on the dimensions of NPs and the size of their agglomerates in dispersion, which are usually present due to CeO_2 poor solubility (Abdi Goushbolagh et al. 2018). In recent decades, researchers have investigated surface modifications that would address the solubility problem. One such modification concerns the coating of NPs with dextran. Dextran molecules have been shown to successfully stabilize the surface charge of CeO_2 NPs and prevent agglomeration, without affecting the redox properties and toxicity of CeO_2 *per se* (Naha et al. 2020; Perez et al. 2008; Yazici, Alpaslan, and Webster 2015; Karakoti et al. 2007).

The most common methods for screening the cytotoxicity of NPs are based on the loss of cell membrane integrity or mitochondrial membrane potential, demonstrating the physical state of the cells, with no insight into the underlying mechanisms. To detect more specific biochemical changes caused by NPs, e.g. DNA degradation or expression of a protein of interest, several standard methods that include labels, dyes or antibodies would be required (Drasler et al. 2017). With some of them NPs can interfere, which makes the result of the experiment irrelevant (Monteiro-Riviere, Inman, and

Zhang 2009). On the other hand, Raman spectroscopy gives an insight into the entire chemical composition of the cell and the structures of present biomolecules (Ferraro, Nakamoto, and Brown 2003). Physiological or pathological changes in the cell that lead to a change in its biochemical composition are reflected in the cell's Raman spectrum (Brauchle et al. 2014; Shin et al. 2019; Wieland et al. 2021; Short et al. 2005; Lasalvia, Perna, and Capozzi 2019). Since the Raman spectrum of a NP-treated cell contains information about the effect of NPs on numerous cellular macromolecules, it can be used to simultaneously monitor several changes, for which several conventional biological methods are usually needed. Furthermore, Raman spectroscopy is a non-destructive, biocompatible method that does not require additional chemicals and labels. Consequently, Raman spectroscopy offers great possibilities in screening and studying the effects of NPs on human cells.

Raman measurements are most often performed on a single cell, which is another advantage compared to conventional methods for evaluating the effects of NPs on the cells (Brauchle et al. 2014; Ma et al. 2021; Pavillon and Smith 2023). Differences in the Raman spectra of NP-treated cells enable monitoring of different modalities of interactions between NPs and the cell and correlate spectroscopic with biochemical and morphological changes (Lasalvia, Perna, and Capozzi 2019; Fazio et al. 2020). For this purpose, Raman images, showing the spatial distribution of spectral information, are of great help (Harvanova et al. 2017; Ahlinder et al. 2013). To assess the effects of NPs on the cell culture as a whole, it is necessary to analyze the Raman spectra of a large number of cells using multivariate statistical methods. In this way, cells can be grouped and classified according to the effects of NPs and finally can be compared with each other. One of the common methods used for this application is principal component analysis (PCA) (Brauchle et al. 2014; Pavillon and Smith 2023; Schie et al. 2014; Crow et al. 2005). In a previous publication, we showed that the relatively new and non-standard method of non-negative PCA (nnPCA) is particularly suitable for the analysis of cells' spectra, since in the resulting components, which show the differences between the analyzed spectra, Raman spectral features of specific molecules are easily recognized (Miletić et al. 2023). Particular attention was paid to the lipid features of the Raman spectrum as potentially important for recognizing the degree of cell damage caused by NPs. Vertex component analysis (VCA) is another unsupervised method of

multivariate statistics. While PCA components represent linear combinations of original variables that capture the variability of the data set in the best way, the VCA algorithm extracts pure components, so-called endpoints, which are differently abundant in each of the original variables (Nascimento and Dias 2005). If Raman spectra are collected at many points across the entire cell, the contribution of each VCA component can be quantified for each point and used to create a color image of the cell. This method is less frequently used than PCA (Mazur et al. 2013; Hedegaard et al. 2011; Krafft et al. 2011; Zuser et al. 2010; Liu et al. 2022) for the analysis of the cells' Raman spectra. There are only few published studies that used VCA for Raman imaging of NP-treated cells, and none of them addressed the cytotoxic effect of NPs (Chernenko et al. 2009; Chernenko et al. 2013; Tolstik et al. 2016).

In this work, the cytotoxic effect of dextran-coated CeO_2 NPs on MRC-5 cells was studied using vibrational Raman spectroscopy. To the best of our knowledge, there is no data in the available literature on the effect of dextran or similar material coated CeO_2 NPs on MRC-5 cells. Dose-dependent differences among cell spectra were analyzed primarily using nnPCA. Raman spectra combined with PCA and VCA were also used to obtain Raman-PCA/Raman-VCA images, showing the differences in the spatial distribution of biomolecules of control and treated cells. In addition to Raman spectroscopy, several conventional biological methods were employed to detect changes in cell growth, metabolic activity and induction of apoptosis in NP-treated MRC-5 cells. The performed experiments aimed to expand knowledge about safety issues related to the use of CeO_2 NPs in industry and medicine, applying for this purpose a comprehensive approach of Raman spectroscopy and at the same time examining the potential of the given methodology in this scientific field.

2. Materials and methods

2.1. Cell culture

MRC-5 cells (ATCC, USA), human fetal lung fibroblasts, were cultured in DMEM high glucose content medium (Sigma-Aldrich, USA) supplemented with 10 % fetal calf serum (FCS, Sigma-Aldrich) (v/v) and 1 % antibiotic/antimycotic solution (Sigma-Aldrich), in a humidified atmosphere with 5 % CO_2 at 37∘C.

MRC-5 is a normal diploid human cell line with a 46, XY karyotype, derived from normal lung tissue

of a 14-week-old male embryo (Jacobs et al., 1970). The modal number of chromosomes is 46 and occurs in 70 % of cells, with the polyploidy rate of 3.6 %. Cells are capable of 42 to 46 population doublings before senescence begins. MRC-5 cells display a fibroblast-like morphology, with a diameter of approximately 18 µm. Doubling time can vary between 35 and 45 hours, depending on cultivation conditions. MRC-5 cells used in this study were between 25 and 30 population doublings (ATCC n.d.; Cytion n.d.).

2.2. NPs synthesis and cell treatment

Dextran-coated CeO_2 (CD) NPs were synthesized according to the synthesis procedure by Karakoti et al (Karakoti et al. 2007). Briefly, 0.5 g of cerium nitrate hexahydrate was added in 50 ml of 0.135 mM dextran T40 solution in deionized water. The resulting solution was oxidized with 0.05 ml of 30 % ammonia and stirred for 24 hours. 24 hours after cell seeding, the cell culturing medium is replaced with a fresh medium containing 100 µg/ml, 200 µg/ml or 400 µg/ml CD NPs and incubated for 48 hours. Synthesized NPs were stable in dispersion, with an average grain size of 3–4 nm and the hydrodynamic radius of 47 nm (Miletić et al. 2020).

2.3. NPs characterization

The grain size of NPs was estimated using transmission electron microscopy, while crystalline structure and average crystallite size was determined from X-ray diffraction (XRD) spectra, as described in our previous study (Miletić et al. 2020). The specific surface area and porosity of the nanoparticles were determined using a gas-adsorption analyzer, SURFER ANALYZER 11510300 (Thermo Fisher Scientific). Before measuring, the powder samples were degassed under vacuum (10^{-2} Torr) at 150 °C for 2 hours to remove any adsorbed gases. The Brunauer-Emmett-Teller (BET) analysis method was employed to calculate the specific surface area. Average hydrodynamic radius of NP was determined by dynamic light scattering (DLS), also described earlier (Miletić et al. 2020).

2.4. SRB assay

Cells were cultured in 96-well plates with seeding density of 7000 cells/well. Next day the cells were treated with CD NPs, incubated for 48 h and then

fixed with trichloroacetic acid. After fixation, the cells were stained for 15 min with 0.4 % (wt/vol) sulforhodamine B (SRB) (Sigma-Aldrich) dissolved in 1 % acetic acid. Washing with 1 % acetic acid repeated in four steps was applied to remove unbound dye. SRB which stayed bound was extracted with 10 mM unbuffered Tris base (Sigma-Aldrich). The absorbance of the extracted dye solution was measured at 550 nm in a microplate reader (Wallac, VICTOR2 1420 Multilabel counter, PerkinElmer, Finland). The absorbance values obtained for NPs without the cells (blank) was subtracted from the values obtained for samples. Results were presented as percent of the control, where the cell growth of control is set to 100 %, in the form of mean values ± standard error. The assay was performed three times in three replicates for every experimental group. Statistical significance of differences between treated and untreated cells was estimated by one-way analysis of variance (ANOVA) and *post-hoc* Tukey test, performed in R.

2.5. MTT assay

Cells were seeded in 96-well plates at density of 7000 cells/well and next day treated with CD NPs. After 48 h, the cell culture medium with NPs was discarded and 100 µl of fresh culture medium containing 0.5 mg/ml of MTT (Sigma-Aldrich) was added. Upon 2 h of incubation at 37 °C and 5 % CO_2, 100 µl of 10 % SDS (0.01 N HCl) was added to each well and the plate was incubated at 37 °C overnight. The absorbance was measured at 570 nm on a microplate reader (ELx800, BioTek). Results were calculated by subtracting absorbance values obtained for blank (NPs without the cells) from the values obtained for samples and the average value for the control cells (cells without NPs) was set to 100 %. Results were presented as percent of the control. Experiments were repeated three times in three replicates. The data are presented as mean ± standard error. One-way ANOVA with Tukey *post-hoc* test performed in R was used for statistical analyses since the data followed a normal distribution.

2.6. Apoptosis detection

For apoptosis detection, a commercial FITC Annexin V Apoptosis Detection Kit with PI (Biolegend, USA) was used. The protocol given by the manufacturer was adapted for staining on microscope slides. The cells were grown for 48 h on 20×20 mm glass slides in a cell culture medium, after which the medium

was removed. The slides were rinsed twice with PBS and immersed in annexin-V binding buffer with annexin-V-FITC (5 µl/100 µl of buffer) and propidium iodide (PI; 10 µl/100 µl of buffer) added. After 15 min of incubation at room temperature in the dark, slides were rinsed twice in PBS and air dried. In the final step of sample preparation, microscope cover slips were mounted to slides with the aid of mounting medium Mowiol (Sigma-Aldrich). The samples were analyzed by Leica TCS SP5 II confocal microscope (Leica Microsystems, Germany), equipped with acusto-optic tunable filter and acusto-optic beam splitter for excitation-emission separation. The emitted radiation of various wavelengths is taken to two photomultiplier tubes for detection. Visualization was achieved by excitation of FITC with 488 nm Ar laser and PI with 543 nm HeNe laser. The emitted fluorescence was detected in sequential mode via the green (FITC) and red (PI) channels, to avoid signal overlap between the channels. Samples with untreated cells that underwent exactly the same staining and preparation procedure as treated cells were used as negative controls. At least six fields of view were recorded from each sample.

For assessing the frequency of apoptotic cells by flow cytometry, the same FITC Annexin V/PI kit was used, following the manufacturer's instructions for flow cytometry. In brief, untreated MRC-5 cells and cells incubated with NPs for 48 h were washed twice in PBS supplemented with 2 % FCS and 0.01 % NaN_3 (Sigma-Aldrich Chemie GmbH), and resuspended in Annexin V Binding Buffer. Next, 5 µL of FITC-conjugated annexin V and 10 µL of PI solution were added to the cells and incubated for 15 min at room temperature in the dark. For analysis, 50 000 events per sample were acquired on a flow cytometer (LSR II, Becton Dickinson, East Rutherford, NJ, USA). Data were analyzed using FlowJo v10 software (TreeStar Inc., Achland, OR, USA). One-way ANOVA with Tukey *post-hoc* test was used for statistical analyses.

2.7. Transmission electron microscopy (TEM)

NP-treated cells after 24 hours of incubation, as well as untreated controls were detached from the cell flask surface using trypsin/EDTA, washed twice with PBS and fixed in 2.5 % glutaraldehyde in 0.1 M cacodylate buffer. Cells were then post-fixed with 1 % osmium tetroxide in the same buffer, dehydrated in a series of ethanol and embedded in Epon (Agar Scientific, UK). The sections were cut with a diamond knife (Diatome, Switzerland), mounted on

copper grids and counterstained with uranyl acetate and lead citrate on Leica EM STAIN (Leica Microsystems, Germany). Philips CM12 transmission electron microscope (Philips/FEI, The Netherlands) operated at 60 keV and equipped with a SIS MegaView III digital camera (Olympus Soft Imaging Solutions, Germany) was used for examination and images obtaining.

2.8. Raman spectroscopy

For the Raman experiments, three sample groups were prepared: cells treated with 200 µg/ml CD NPs, cells treated with 400 µg/ml CD NPs and control cells. Each group was grown in three T-25 cell culturing flasks in parallel, i.e. in three replicates. After incubation with NPs, treated cells, as well as untreated controls, were detached with trypsin/EDTA. During the step of inhibition of trypsin, cell suspensions from three cell flasks of the same sample group were collected into one common tube. After removing the trypsin, the cells were fixed in Roti-Histofix 4 % (Roth, Germany) for 20 min at room temperature and washed twice in PBS (2 × 5 ml per flask). The resulting pellets were resuspended in 1 ml of PBS and stored at 4 °C. Right before the measurement, PBS was discarded, the cells were washed in 1 ml of DI water and resuspended in 50 µl of DI water (100 µl for control sample, due to higher cell density). A drop of 20 µl was placed onto CaF_2 coverslip and air dried. Raman spectra were acquired with NT-MDT system NTEGRA Prima (NT-MDT, The Netherlands) using 600 g/mm grating. A laser excitation line of 532 nm with an incident power of ~0.5 mW was used and the exposure time was 180 s. Raman spectra were measured in the nuclear region of the cell, to avoid spectral differentiation based on different cell compartments. The cells chosen to be measured were not selected based on their morphology but randomly chosen.

2.9. Raman spectra preprocessing

The obtained spectra were calibrated using Raman spectra of paracetamol. The spectral region (700–1800) cm^{-1}, so called fingerprint region, was chosen for the analysis. The background was subtracted by first order polynomial fit. Finally, Raman spectra were normalized relative to the mean intensity calculated for entire spectrum. All spectral preprocessing steps were performed in R, using hyperSpec package (Beleites and Sergo 2024).

2.10. Raman data analysis

nnPCA was performed in R using *nsprcomp* package (Sigg 2018). The function of the same name, *nsprcomp*, computes components (nnPCs) by projecting the principal vectors onto the non-negative orthant. Each nnPC is calculated after the previous one so that it captures the maximum of variance not explained by the previous nnPCs. The procedure would be the same as standard PCA if the negativity restriction were not applied. The percentage of the explained additional variance of each nnPCA is calculated using function *peav*.

K-means clustering was performed using the function *kmeans* from the R package *stats*. The goal of this method is to group the data of the dataset into clusters, in such a way that the sum of squares from each data point (a spectrum) to the centroid of the cluster is minimized. The number of clusters should be predefined. Here, the grouping of all measured Raman spectra (control and treated cells' spectra) into four clusters was chosen. Clustering into three and five groups was also tried out but gave less valid physical meaning.

2.11. Raman imaging

Cell samples for Raman imaging were prepared in the same way as for previously described Raman measurements (Paragraph 2.8). Two sets of samples were prepared: cells treated with 200 µg/ml CD NPs and control (untreated) cells. Micro-Raman spectroscopy investigation of the individual cells was performed on confocal Horiba Xplora plus system equipped with 532 nm laser excitation source and Peltier cooled CCD detector. The Raman spectra were collected with low laser power, using 50x long working distance (LWD) objective and 600 g/mm grating.

To map single cells, we utilized a piezo-controlled sample stage, adjusting the grid raster to match the morphology of the cells under investigation. Data acquisition was performed within the spectral range of 500 cm^{-1} to 1800 cm^{-1}, with each acquisition lasting 30 seconds. Following the measurements, we applied a first order polynomial baseline fitting procedure to all collected spectra. This step was crucial for compensating for random spatial variations on the sample surface.

Subsequently, PCA analysis of measured spectra in the region 700 cm^{-1} to 1800 cm^{-1} was performed for each single cell (NP-treated and control), using R function *prcomp* from package *stats*. The resulting

PC1 was used for cell imaging: PC1 score values for each pixel were presented by color scale (from green to red). Similarly, the VCA imaging method was applied: based on the abundance of VC1, VC2 and VC3 components in the spectra of each pixel, color maps of both control and treated cells were created. This method was applied using R function *vca* from package *hyperSpec.utils*, with *ncomp* argument set to value 3 (for extraction of three pure components from the data set) (Mayer 2024). Spectra measured on the cell periphery were excluded from both PCA and VCA imaging, due to the significantly different background and signal-to-noise ratio. If they were included in the analysis, they would be separated into distinct group as outliers, masking the differences between the spectra measured on the central part of the cells. For that reason, we first did PCA to identify such outliers and then repeated PCA or performed VCA with the rest of the spectra. In that way we have imaged ~500–600 pixels for control and NP-treated cells, with a pixel size of $0.6 \times 0.6\,\mu m$.

3. Results and discussion

MRC-5 cells grown in culture were treated with CD NPs synthesized and characterized in our previous study (Miletić et al. 2020). They proved to be very stable in dispersion, with a hydrodynamic radius of less than 50 nm, while the CeO_2 NPs used in previous studies on MRC-5 cells were very susceptible to agglomeration, with a hydrodynamic radius of at least 500 nm (Pešić et al. 2015; Spezzati et al. 2017; Alghamdi 2023; Abdi Goushbolagh et al. 2018). The average grain size, crystallite size, hydrodynamic radius and specific surface area (SBET) of CD NPs are summarized in Table 1 (more details are given in Supplementary material and Figure S1).

CD NPs were applied in the dose range of (100–400) μg/ml, also used in previous studies of CeO_2 NPs effect on MRC-5 cells (Pešić et al. 2015; Spezzati et al. 2017; Alghamdi 2023; Abdi Goushbolagh et al. 2018), with an altered incubation time of 48 hours. The effects of NPs were first evaluated by standard

Table 1. Characteristics of CD NPs: grain size estimated from TEM images; average crystallite size, determined from XRD using Scherrer formula; average hydrodynamic radius, determined by DLS; and BET specific surface area (S_{BET}).

Grain size (TEM)	Crystallite size (XRD)	Hydrodynamic radius (DLS)	Specific surface area (S_{BET})
≈ 4 nm	3.5 nm	46.5 nm	34.4 m²/g

biological methods, in order to select the doses that will be used for Raman measurements based on their results and to assure more reliable interpretation of Raman spectra analysis.

3.1. NPs effects on cell growth, metabolic activity and apoptosis induction

Effects of NPs on cell growth (SRB assay), metabolic activity (MTT) and induction of apoptosis (annexin-V-FITC) were examined. Changes in metabolic activity determined by MTT were more intense than the changes in cell growth detected by SRB assay for the same applied dose of NPs (Figure 1). While average cell growth decreased to 67 % and 29 % in average upon treatment with 200 μg/ml (CD-200 cells) and 400 μg/ml CD NPs (CD-400 cells), respectively, metabolic activity registered by MTT dropped sharply to 32 % and 10 % in average, relative to control. Considering that MTT assay detects the level of metabolic activity based on mitochondrial function preservation, it follows that mitochondrial function impairment is one of the first events in the cells treated with cytotoxic dose of CD NPs. Interestingly, at the lowest applied dose, 100 μg/ml, a slight increase (109 % in average) in metabolic activity is noticed, possibly through the stimulation of cell proliferation. At higher doses, CD NPs are undoubtedly cytotoxic. As previously stated, due to their physicochemical properties, CeO_2 NPs exert both pro-oxidative and anti-oxidative activity, which could result in different, sometimes opposite, effects on cells. Nevertheless, in order to trace the changes of the same parameters, we limited this study to cytotoxic doses of NPs.

Impairment of mitochondrial activity caused by CD NPs leads to induction of cell death, which is confirmed by staining the cells with fluorescently labeled annexin-V and PI. Annexin-V specifically binds to phosphatidylserine, while PI intercalates between the bases of nucleic acids and dyes them. In the confocal microscopy images shown in Figure 2a, left panel, cells stained by annexin-V-FITC only (annexin-V⁺/PI⁻, colored green) represent the cells with externalized phosphatidylserine, but still with the intact cell membrane, i.e. the cells in early apoptosis. The cells stained with both annexin-V-FITC and PI (annexin-V⁺/PI⁺, colored green and red) are the cells with damaged cell membrane, i.e. cells in necrosis or later phases of apoptosis. For quantifying cell frequencies in early and late apoptosis flow cytometry was used. The flow cytometry analysis confirmed that exposure to CD NPs induced apoptotic cell death of MRC cells. Namely, compared to the control cells, 48 h
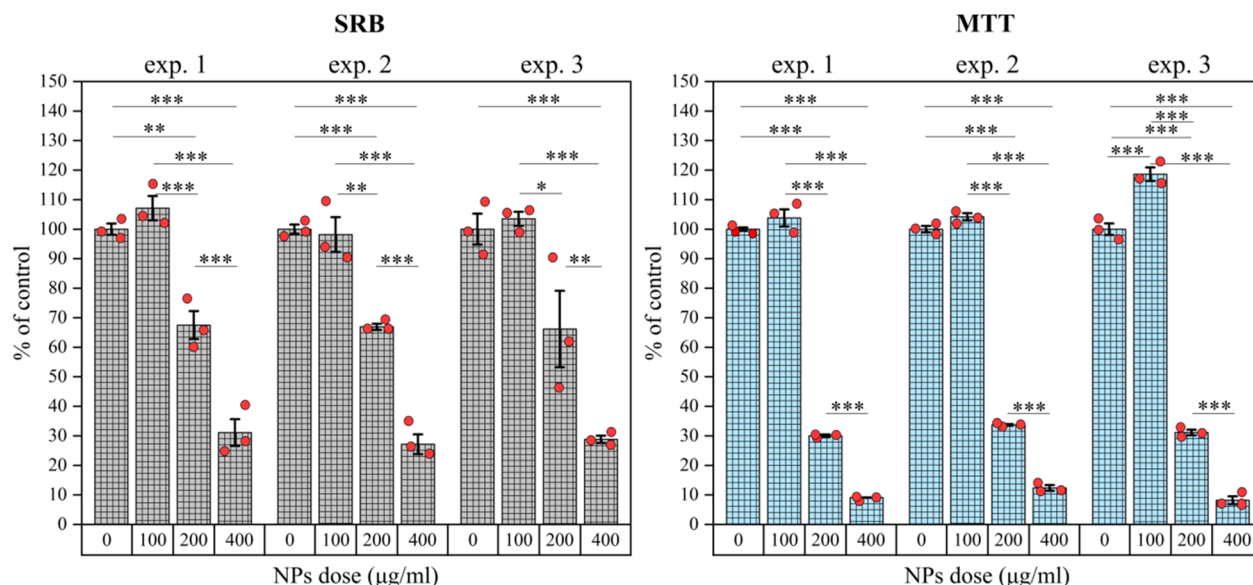
Figure 1. Changes in cell growth (left) and metabolic activity (right) induced by CD NPs, assessed by SRB and MTT assays, respectively. Standard error bars, *p < 0.05, **p < 0.01, ***p < 0.001.

exposure to both CD-200 and CD-400 NPs increased the frequency of early (annexin V^+/PI^-) and late (annexin V^+/PI^+) apoptotic cells in culture. Moreover, the frequency of late apoptotic cells increased in a concentration-dependent manner, whereas the frequency of early apoptotic/necrotic cells was similar among the cells exposed to either CD-200 or CD-400 (Figure 2a, right panel, and Figure 2b).

TEM imaging was performed on treated cells with lower dose of CD NPs, i.e. CD-200 cells, to confirm the uptake and intracellular presence of NPs. TEM images of both control and CD-200 cells are shown in Figure 3. Accumulations of NPs can be detected mostly in cytoplasmic endosome-like vesicles across the entire NP-treated cell, except within the nucleus.

3.2. Raman spectroscopy of NP-treated cells and spectral multivariate analysis

Since biological methods showed that doses of 200 μg/ml and 400 μg/ml CD NPs are both cytotoxic to MRC-5 cells but to a different extent, the Raman measurements were performed on both groups of MRC-5 treated cells, as well as on untreated cells as controls. Raman spectra of treated and untreated MRC-5 cells were comparatively analyzed. In Figure S3 (Supplementary material) mean Raman spectra of control and treated cells are presented. As can be seen, spectral differences between the three cell groups are very subtle and manifested by the changes of relative intensity, rather than by radical decrease/increase of particular Raman modes intensities. The standard deviation for CD-200 cells is the

largest, suggesting the existence of different subpopulations of the cells, with unequal levels of damage.

To extract more precisely changes in the Raman modes in treated cells, nnPCA was applied. This non-conventional modification of standard PCA is useful in the analysis of cell spectra, resulting in PC loadings which could be interpreted more intuitively. nnPCA was performed in a pairwise manner, meaning that CD-200 and CD-400 cells spectra were analyzed separately, through direct comparison with the control. PC components that enable the greatest separation of cell groups, i.e. that best describe the differences between control and treated cells, were identified using PC scores plots. The relevant scores plots for CD-200 and CD-400 cells are shown in Figures 4 and 6, respectively. Corresponding PC loading vectors for CD-200 and CD-400 cells are shown together in Figure 5. The peaks contained by PC loading vectors indicate Raman modes whose intensity changes in the spectra of treated cells, while the sign of PC scores (PC^+ or PC^-) determines the direction of the change (increase or decrease of Raman mode intensity).

As can be seen from Figure 4, nnPCA of control and CD-200 cells abstracted two PCs which segregate control and treated cells: PC1 and PC2. Taken together, those two PCs encompass ~60 % of total variance among the cells spectra. On average, CD-200 cells have a positive PC1 score ($PC1^+$), hence PC1 presents Raman modes whose intensity increases after the treatment with NPs (Figure 5a). For PC2, the reverse is true: CD-200 cells on average
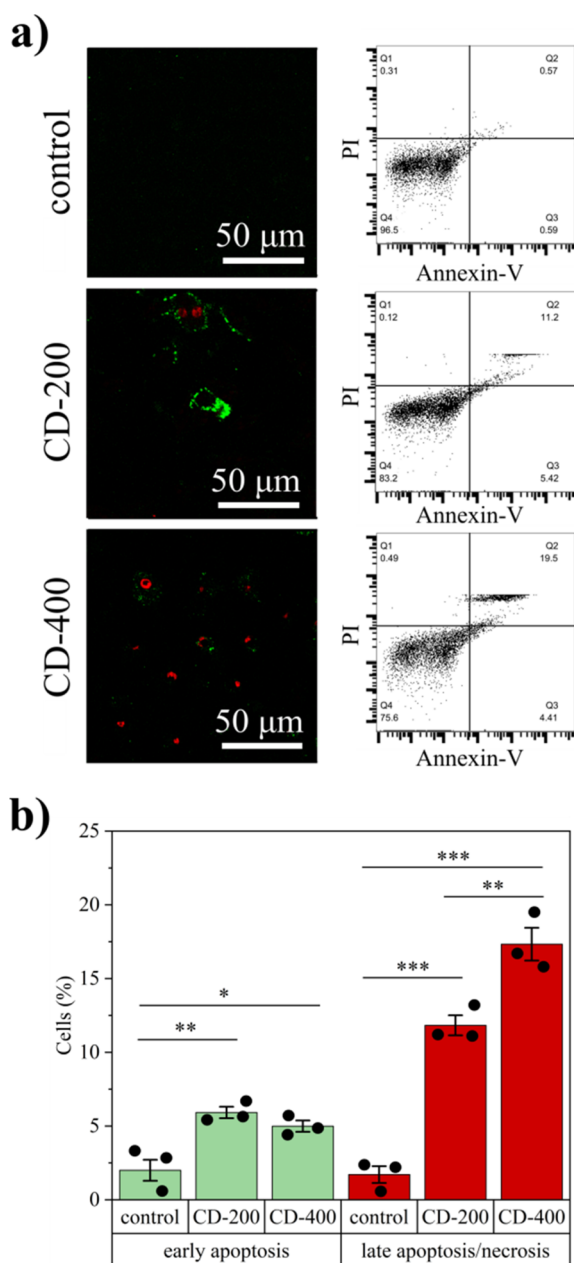
Figure 2. Induction of cell death caused by CD NPs. a) Left panel: fluorescence confocal microscopy images of cells dyed with annexin-V-FITC (green) and PI (red). Annexin-V⁺/PI⁻ (colored only green) are cells in early apoptosis, while annexin-V⁺/PI⁺ (colored green and red) are in late apoptosis or necrosis. Right panel: the corresponding flow cytometry dot plots indicating annexin-V-FITC *vs* PI staining of MRC-5 cells are presented (control cells in the first row and CD-200 and CD-400 treated cells in the second and third rows, respectively). b) Distribution of early (quadrant Q3) and late (quadrant Q2) apoptotic cells, gated as indicated on the flow cytometry dot plots. Standard error bars, *p < 0.05, **p < 0.01, ***p < 0.001. The presented data are from one of two experiments with similar results performed in three technical replicates.

Figure 3. TEM images of the untreated cell (row 1) and the cells treated with CD-200 NPs (rows 2–4). Arrows point to NPs accumulations in the cell. For more images of control cells see Figure S2 in Supplementary material.

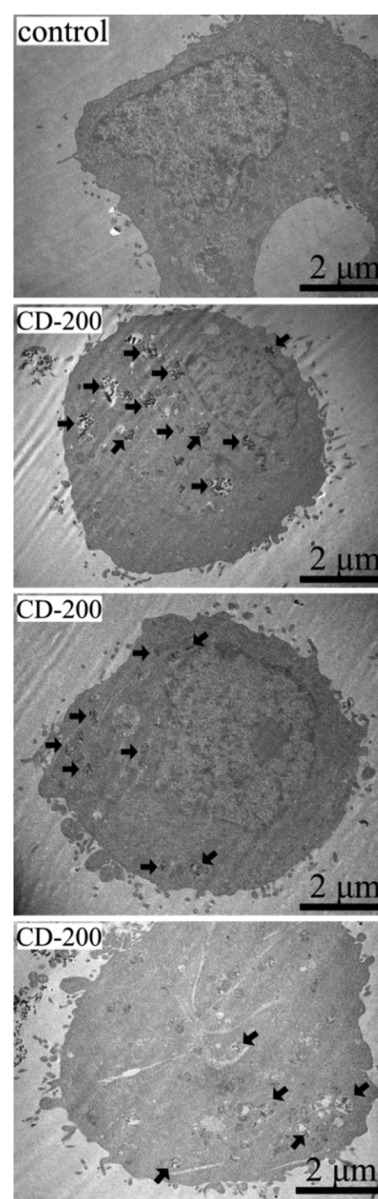have a negative PC2 score sign (PC2⁻), therefore PC2 presents the Raman modes with decreasing intensity in NP-treated cells (Figure 5d). Control cells on average have negative PC1 and positive PC2 scores (PC1⁻/ PC2⁺); the corresponding annotation will be used for the other PCs in the further text.

PC1 overall appearance from Figure 5a resembles the Raman spectrum of lipid molecules and almost all presented peaks can be assigned to different types of lipid modes, though other biomolecules cannot be strictly excluded. In Table S1 (Supplementary material) are presented cell Raman modes assignations. Furthermore, all peaks present in this component, except 1128 cm⁻¹, 1147 cm⁻¹, 1162 cm⁻¹, 1548 cm⁻¹ and 1597 cm⁻¹ peaks, are contained in the Raman spectrum of phosphatidylserine (Milligan et al. 2021).

PC2 resulting from the same analysis is shown in Figure 5d. Considering the negative PC2 score sign for CD-200 cells, all peaks that appear in this component indicate the decreasing intensity of corresponding Raman modes. PC2 is composed of typical nucleic acid modes: 786 cm⁻¹, 1099 cm⁻¹, 1182 cm⁻¹, 1375 cm⁻¹, 1485 cm⁻¹ and 1576 cm⁻¹. The presence of a small shoulder at 814 cm⁻¹, as well as the position of the mode at 1099 cm⁻¹ instead of 1095 cm⁻¹, suggest that RNA molecules are present among the nucleic acids which diminish in CD-200 treated cells. Also, for the peaks centered at 1237 cm⁻¹ and 1337 cm⁻¹, the shoulders positioned at ~1245 cm⁻¹ and 1322 cm⁻¹, which are particularly prominent in RNA (Samuel et al. 2022), are hinted. Beside nucleic acids modes, this PC2 contains a few peaks typical
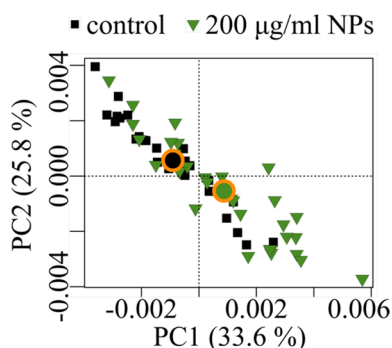

Figure 4. nnPCA of control (black squares) and CD-200 cells (green triangles): PC1:PC2 scores plot. Centroids of the groups are represented by a correspondingly colored circles with an orange border. Percentages in the brackets denote the amount of total variance encompassed by each PC.

for protein Raman modes (1006 cm⁻¹, 1162 cm⁻¹, 1683 cm⁻¹). Modes at 1237 cm⁻¹ and 1337 cm⁻¹ could be from protein and nucleic acids both (see Table S1).

Results of the Raman spectra analysis by nnPCA method can be explained in the light of the results given by standard biological experiments. A decrease in cellular metabolic activity, that is disordered mitochondrial function, could be caused by oxidative stress generated by CD NPs in the cell, which was reported in previous studies (Hussain et al. 2012; Park et al. 2008). Overproduced ROS induce mitochondrial membrane potential loss and impairment of the mitochondrial oxidative chain, leading to increased mitochondrial membrane permeability and loss of its function. At that step, MTT assay already detects the cytotoxic effect of NPs (Figure 1). Cytochrome C released from dysregulated mitochondria triggers the apoptosis pathway (Figure 2), while disruption of mitochondrial redox reactions leads to the enhancement of oxidative stress and deterioration of oxidative damage of other cell structures and molecules. Beside mitochondria, ROS damage DNA, causing breaks of its chains, which also triggers apoptosis. Therefore, decreased DNA Raman modes, especially those originating from phosphodiester bonds, could be expected as a consequence of oxidative DNA damage. RNA present in the cell is also damaged by ROS, while new RNA transcription is disabled by the degradation of DNA and overall metabolic dysregulation. When apoptosis is triggered in the cells, one of the first biochemical events is an externalization of phosphatidylserine to the outer leaflet of the cell
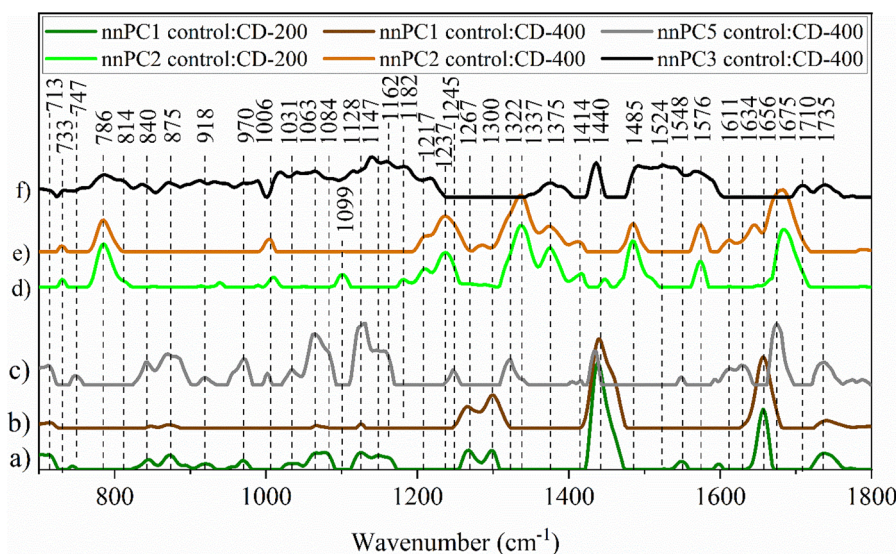

Figure 5. PC loading vectors showing the variations in lipid content among the cells: a) PC1 obtained from nnPCA of control and CD-200 cells, b) PC1 obtained from nnPCA of control and CD-400 cells, c) PC5 obtained from nnPCA of control and CD-400 cells. PC loading vectors showing the variations in nucleic acid content among the cells: d) PC2 obtained from nnPCA of control and CD-200 cells, e) PC2 obtained from nnPCA of control and CD-400 cells, f) PC3 obtained from nnPCA of control and CD-400 cells.

membrane. Externalized phosphatidylserine is therefore conventionally used as a marker for early apoptosis detection, usually by exposing the cells to labeled annexin-V (Figure 2). Detection of early apoptotic NP-treated cells correlates to increased phosphatydylserine Raman modes in treated cell spectra. Other lipid structures in treated cells which can be associated with increased lipid Raman modes, are different membranous organelles, such as endosomes or endolysosomes, generated by NPs intake, or lipid droplets, overaccumulated in cell death processes.

The changes in the Raman spectra of CD-200 cells (Figure 5a and d), correspond very well with the results obtained by standard biological assays. The resemblance of nnPC components to the Raman spectra of particular biomolecules (lipids and nucleic acids) makes spectral analysis of CD-200 cells relatively simple.

However, with the higher dose of NPs (CD-400), the analysis becomes slightly more complex. Figure 6a and b present PC scores obtained from nnPCA of control and CD-400 cells. The upper score plot shows that treated and untreated cells can be best distinguished by PC1 and PC5, though separation by PC1 is much greater: more than 90 % of analyzed

Figure 6. nnPCA scores plots of control (black squares) and CD-400 cells (brown triangles): PC1:PC5 (a) and PC2:PC3 (b). Centroids of the groups are represented by a correspondingly colored circles with a green border. Percentages in the brackets denote the amount of total variance encompassed by each PC. The cells with positive PC1 but negative PC5 score values (PC1$^+$/PC5$^-$ cells) are encircled by a black curve at the upper graph; the same cells at the bottom graph are encircled also with black curves.

treated cells differ from control. This component also encompasses much larger part of the total variance than PC5. Corresponding PC1 and PC5 loadings are shown in Figure 5b and c, respectively.

Like PC1 from the analysis of cells treated with lower dose of NPs, this PC1 also shows an increase in lipid modes intensity in treated cells. The difference in lipid content between treated and control cells, based on PC1, is more emphasized for the higher than for the lower dose (compare Figures 4 and 6 a). This could be partially attributed to the increased level of endocytic vesicles, more present at higher doses. The appearance of PC1 difference among the two doses (Figure 5a and b) seems to be of particular interest. The most obvious difference is in the relative intensity of 1267 cm^{-1} and 1300 cm^{-1} peaks, I_{1267}/I_{1300}, which is significantly higher for the cells treated with the lower dose of NPs (Figure S4, Supplementary material). According to the literature, higher intensity ratio of these modes in the Raman spectra of cells indicates lower saturation of cellular lipids (Czamara et al. 2015). Our previous study pointed to this intensity ratio as a potential marker indicating the degree of NP-induced cell damage (Miletić et al. 2023). This study confirms that I_{1267}/I_{1300} has a higher value in early apoptotic cells, compared to the cells in late apoptosis or necrosis.

Furthermore, PC1 obtained from the analysis of higher dose (Figure 5b) is less rich in resolved peaks and almost without peaks in the region (800–1000) cm^{-1}, typical for phospholipids. Instead, phospholipid modes from this region appear in PC5 (Figure 5c), which also has positive score sign for treated cells (PC5$^+$). In PC1:PC5 score plot (Figure 6a) the following can be observed: while almost all treated cells differ from control by PC1, most of them, but not all, differ also by PC5. Those cells in which total lipid content is increasing (PC1$^+$), but markers of phosphatidylserine and other phospholipids are not expressed (PC5$^-$) are circled by a black curve in the score plot, in order to trace their behavior regarding PC2 and PC3 components. Besides lipid modes, PC5 contains some protein modes too.

PC2 component, bearing mostly DNA Raman modes (Figure 5e), does not separate control and CD-400 cells (Figure 6b). Still, it can be observed that the dispersion of DNA content among treated cells is wider than among control cells: there are cells having lower or higher DNA content than either control cells. It can be assumed that the intensity of DNA Raman signal is under the influence of DNA quantity, integrity and density;
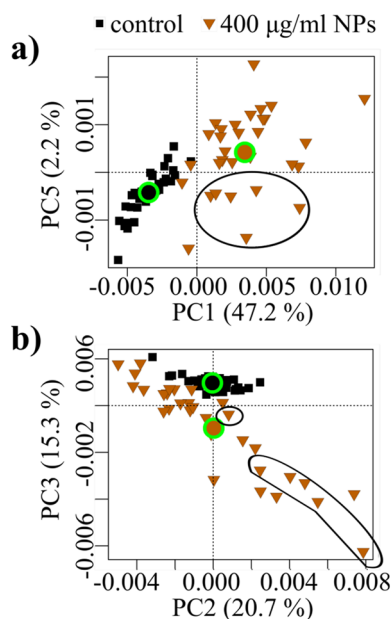
therefore it can be diminished by DNA cleavage, but also enhanced by DNA condensation (Brauchle et al. 2014; Corfe, Dive, and Garrod 2000).

Unlike PC2, PC3 component from analysis of CD-400 cells separates treated from control cells (Figure 6b). This component also bears some of the nucleic acid modes (Figure 5f), but it indicates their decrease upon cell treatment. The most important modes are $786\,cm^{-1}$ and $814\,cm^{-1}$, but also $733\,cm^{-1}$, $1182\,cm^{-1}$, $1237\,cm^{-1}$, $1337\,cm^{-1}$, $1375\,cm^{-1}$, $1485\,cm^{-1}$ and $1576\,cm^{-1}$. Relative intensity I_{814}/I_{786} in this component is particularly high and indicates that the content of RNA rather than DNA diminishes in the cell. Considering that apoptotic nuclear content can be cleaved or highly condensed, while cytoplasmic RNA is degraded, such results of Raman spectra analysis, representing decrease of Raman RNA modes intensity, are in accordance with the previous conclusion.

Treated cells with high nucleic acid content in general (PC2+), but with lower RNA content compared to control (PC3−) are seen in the score plot in Figure 6b. All cells that have a higher lipid (PC1+) but not phosphatidylserine content (PC5−) also belong to this group of treated cells and are marked with the black curve in Figure 6b.

There is, therefore, a population of CD-400 cells in which the lipid content is increased compared to the control (PC2+/PC3−), but also the DNA content (PC1+/PC5−), which is an unusual phenomenon that did not occur with CD-200 cells, nor has it been described in previous studies on NP-treated cells by Raman spectroscopy. At the same time, lipids in the given CD-400 cells were not characterized by phospholipid features, and the content of RNA was reduced compared to the control cells. In order to examine whether PC2+/PC3− and PC1+/PC5− cells underwent specific changes induced only by the highest dose of NPs, the k-means clustering method was applied. This analysis included control, CD-200 and CD-400 cells altogether. The goal was to determine whether among all examined cells, PC2+/PC3− and PC1+/PC5− CD-400 cells would be segregated into a separate cluster. The k-means clustering method requires the number of resulting clusters to be set as an input parameter. Based on theoretical knowledge, it was assumed that cells can be divided into four clusters: unchanged (control) cells, cells in early apoptosis, cells in late apoptosis or necrosis, and cells in some other modality of cell death, characterized by very small reduction of DNA material and an increase in lipids without phosphatidylserine markers. As a result of this analysis, the examined cell spectra were divided into four clusters (Figure 7a), where indeed the spectra of PC2+/PC3− and PC1+/PC5− cells belonged exclusively to one cluster, i.e. cluster 4 (Figure 7a, brown stars). Bar plots in Figure 7b show the composition of each cluster. Most of the control cells belonged to the cluster 3 and a smaller part to the cluster 1. Approximately half of the CD-200 cells belonged to the cluster 3 and half to the cluster 1. Therefore, it was assumed that the cluster 3 contains unchanged cells, while the cluster 1 contains cells in early apoptosis. Cluster 2 contains only two CD-200 cells and more than half of CD-400 cells, therefore it can be assumed that it represents cells in late apoptosis or necrosis. Cluster 4 consists exclusively of a certain number of CD-400 cells. Spectra that correspond to the centroid of each cluster are provided in Supplementary material (Figure S5), along with optical images of the cells positioned closest to each centroid (Figure S6). To analyze spectral differences among the clusters, intensities of typical lipid (I_{1300}) and typical DNA (I_{786}) Raman modes in four centroid spectra were compared. The values are shown in Figure 7c. The cells of cluster 4 have nucleic acids content slightly lower than the control but higher than the cells assumed to be in early and late apoptosis. The lipid content of the cells in cluster 4 is very high, approximately equal to the cells in late apoptosis (Figure 7c). Therefore, it seems more likely that these cells are in some alternative modality of cell death, rather than in the furthest stages of apoptosis or necrosis.

There is a study which showed that at high doses of CeO_2 NPs, in addition to the increased level of apoptosis, the percentage of autophagic cells also increases (Hussain et al. 2012). At low, non-cytotoxic doses, autophagy was not detected. On the other hand, another study shows that autophagic cells are hardly distinguishable from control cells by Raman spectra (Rangan et al. 2018). In the case of cells treated with CD NPs, a large difference in the amount of lipids compared to the control can certainly come from a large number of endocytic vesicles by which the NPs were introduced into the cell, but also from a large number of resulted autophagosomes. Unlike apoptotic cells, autophagic cells are not characterized by externalized phosphatidylserine. In accordance with the above stated, the assumption that CD-400 cells with increased lipid content and not highly reduced nucleic acid content (compared to the control) can represent cells in autophagy is not unfounded. High concentration of NPs could activate autophagy as a protective mechanism, which in the
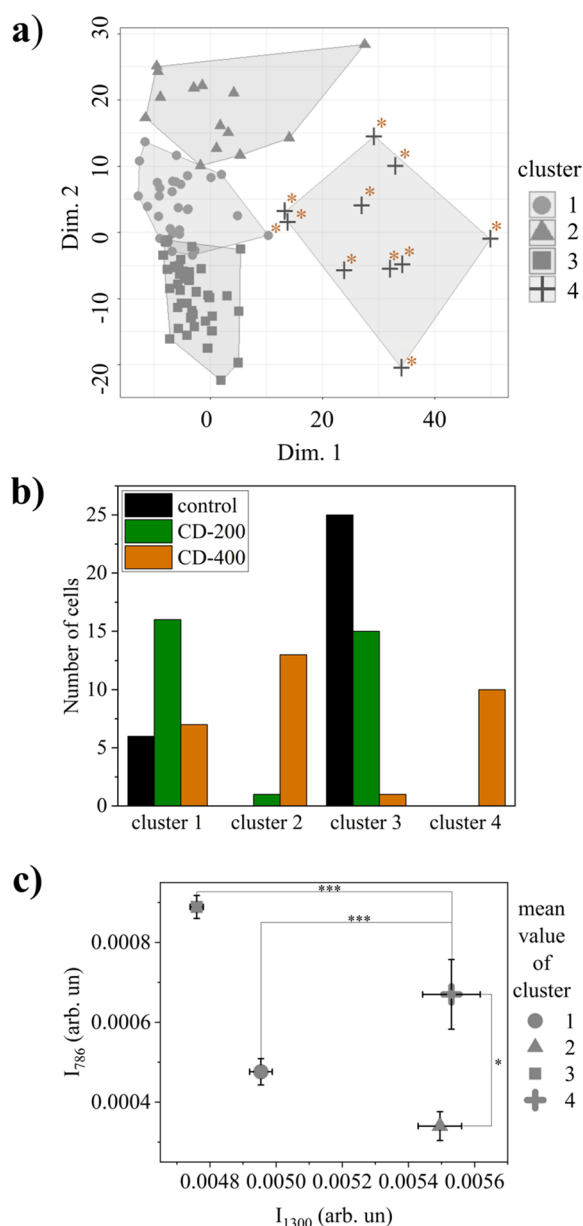
Figure 7. K-means clustering of control and treated cells Raman spectra. a) Four clusters with belonging cell spectra. PC1⁺/PC5⁻ and PC2⁺/PC3⁻ cells are marked with brown stars. b) The composition of each cluster. c) Plot showing Raman intensities I_{1300} (lipids) and I_{786} (nucleic acids) for each cluster and standard error bars. Lines parallel with x-axis and y-axis present statistical significance of differences between the clusters in x (I_{1300}) and y (I_{786}) values, respectively (nonparametric ANOVA, ***$p < 0.001$, *$p < 0.05$).

final outcome can lead to cell death. It is known that the mechanisms of apoptosis and autophagy communicate in the cell in a complex manner (Hussain et al. 2012; Mariño et al. 2014). Cells detected by Raman spectroscopy as members of a separate cluster may therefore be cells that managed to survive the impact of NPs thanks to autophagy, at least until the moment of examination.

It should be noted that proposed distribution of cells in different phases or modalities of cell death, based on the k-mean clustering of cells' Raman spectra, is not entirely consistent with the frequency of apoptosis detected by flow cytometry, though NP dose-dependent increase of late apoptosis frequency is indicated by both methods. Moreover, the percent of NP-treated cells in which changes were detected by Raman spectroscopy is significantly higher than the frequency of apoptosis detected by flow cytometry. Raman spectroscopy certainly captures a wider spectrum of changes in the cells caused by NPs than the externalization of phosphatidylserine and the appearance of cell membrane permeability. Some of them are related to the entry and transport of NPs in the cell and to the direct and indirect interactions of NPs with cellular molecules, which do not necessarily result in apoptosis. On the other hand, MTT assay showed a very large decrease of viability of NP-treated cells, consistent with Raman spectroscopy. Markers of various biochemical changes are intertwined in the Raman spectrum of the NP-treated cell and provide a unique representation of its physiological state. The possibility that Raman fingerprint can indicate lethal changes caused by NPs earlier or more completely than some of the conventional methods used for this purpose should not be overlooked.

3.3. Raman imaging

Raman imaging is usually performed using the intensity of one or more Raman modes in a certain number of locations on the sample to generate an image or map of the sample, where the intensity of the color corresponds to the intensity of a given Raman mode. In this work, instead of classical methodology, the imaging based on multivariate (PCA or VCA) analysis of Raman spectra was used. The goal of combining statistical methods with Raman imaging was to distinguish spectral characteristics across the analyzed cells more clearly. For this reason, we labeled the applied methods as PCA-Raman imaging and VCA-Raman imaging.

The imaging experiments aimed to show NP-induced changes in the spatial arrangement of cell molecules. For this purpose, CD-200 cells were selected, as moderately damaged NP-treated cells which largely kept their integrity, so their maps are more comparable to those of control cells. Raman spectra were measured in each pixel of three control and three CD-200 cells and PCA was applied to all measured spectra of six cells together. The resulting
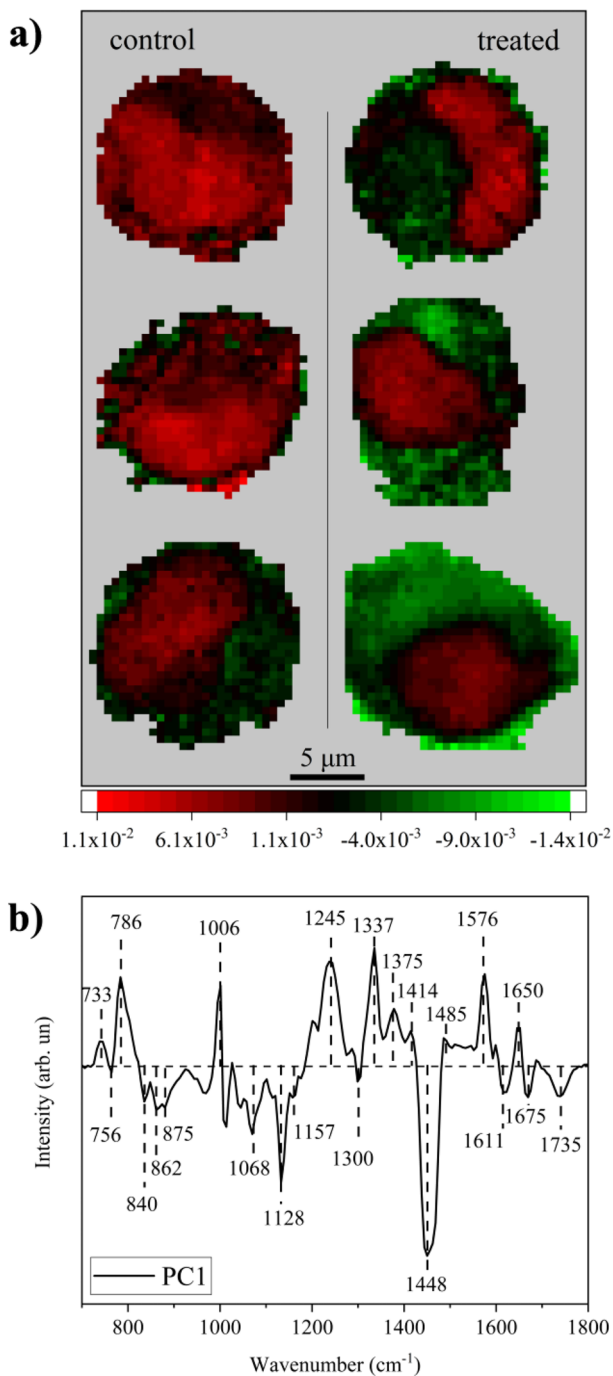
Figure 8. PCA-Raman imaging of control and CD-200 treated cells a) PCA-Raman images of analyzed cells, based on PC1 score values in each pixel (left column – control cells, right column – NP-treated cells); b) PC1 loading spectrum. Local maxima of PC1 are assigned to nucleic acids' and proteins' Raman modes while local minima are assigned to lipid Raman modes, which imply that positive score values at images characterize pixels with high nucleic acids but low lipid content (red) and negative score values characterize pixels with low nucleic acids but high lipid content (green).

PC1 was used to create PCA-Raman images of the cells. Results of this experiment are presented in Figure 8. PCA-Raman images are shown in Figure

8a. PC1 loading spectrum, used for imaging, is shown in Figure 8b. It reflects Raman modes of nucleic acids and proteins as local maxima and lipid modes as local minima (Table S1, Supplementary material). It should be noted that, in this case, standard PCA was used instead of nnPCA, in order to simplify the presentation of both lipid and nucleic acid changes in the same image. PCA-Raman images are generated based on PC1 score value for each pixel on the image, in the way that the highest positive score is represented by light red and the highest negative by light green color (color scale in Figure 8a). Hence, light red pixels denote Raman spectra with high intensity of nucleic acid and protein modes (maxima) but low intensity of lipid modes (minima), while light green represents the opposite: Raman spectra with high intensity of lipid and low intensity of nucleic acid and protein modes. It is interesting that Raman mode at $1006\,cm^{-1}$, assigned to phenylalanine, which is probably the most typical Raman mode of proteins, shares trend in spatial distribution with nucleic acids and not with lipids, although proteins are present together with lipids in the membranes of endocytic vesicles and definitely the smaller portion of total cell proteins is localized in nucleus (Itzhak et al. 2016).

By observing obtained PCA-Raman maps, it can be seen that in control cells, Raman modes of nucleic acids and proteins dominate, occupying the majority of the cell area (Figure 8a, left). They should be most intense in the nuclear region, the edges of which are not clearly defined in the first two control cells. Outside the nucleus, the presence of Raman modes with positive intensity in PC1 may originate from RNA molecules or possibly from mitochondrial DNA. In the third control cell (Figure 8a, third row left), the nucleus is more clearly distinguished, but the intensity of lipid Raman modes, i.e. the lipid content of the cell, is still low. On the other hand, in treated cells, lipids are significantly abundant, as evidenced by the presence of light green dots on the map, while the nuclear region is clearly limited to a smaller area than in control cells (Figure 8a, right). Since these cells, according to the MTT test, are metabolically less active than control cells, reduced transcriptional activity, and thus the amount of RNA and protein in the cytoplasm is expected for them. Also, the increase in the amount of lipids is consistent with endocytosis and demonstrated induction of apoptosis in the treated cells.

In addition to PCA, the VCA method is also applied for Raman imaging. The aim of this method is to extract spectra of pure components from the

mixture of components constituting the sample. Biomolecules that are contained in a cell have many common Raman modes and most often together form different supra-molecular structures. Thus, it is likely that there are no points in the cell that contain perfectly pure components. However, it is expected to obtain components in which the spectral characteristics of certain molecules are more prevalent than others. It was reasonable to expect that components representing lipids, nucleic acids and proteins, as the three main groups of biomolecules in the cell, could be extracted. For that reason, VCA algorithm is designed to calculate three VCA components (VC1, VC2, VC3). VCA is applied to spectra/pixels of each control or CD-200 cell separately. This analysis is performed on the same cells used for PCA-Raman imaging. Results for one control and one treated cell (cells whose PCA-Raman images are shown in the first row in Figure 8a) are

presented in Figure 9. Extracted VCA ('pure') components are given in the first row for control cell (Figure 9a–c) and in the fourth row for CD-200 cell (Figure 9j–l), while corresponding VCA-Raman images are given in the second row for the control (Figure 9d–f) and in the third row for the CD-200 cell (Figure 9g–i). For components representing mostly DNA (VC1) and lipid (VC3) Raman modes, red and green colors are used, respectively. Other two colors are used for VCA components proposed to be dominantly RNA (blue) and dominantly cytochrome c (apricot orange). The intensity scale is denoted on the right side of each image and refers exclusively to a given image.

As expected, in both control and CD-200 treated cell, two VCA components with pronounced nucleic acid (VC1, Figure 9a and j) and lipid Raman markers (VC3, Figure 9c and l) were extracted. In this case, nuclear area in control cell is equally well defined
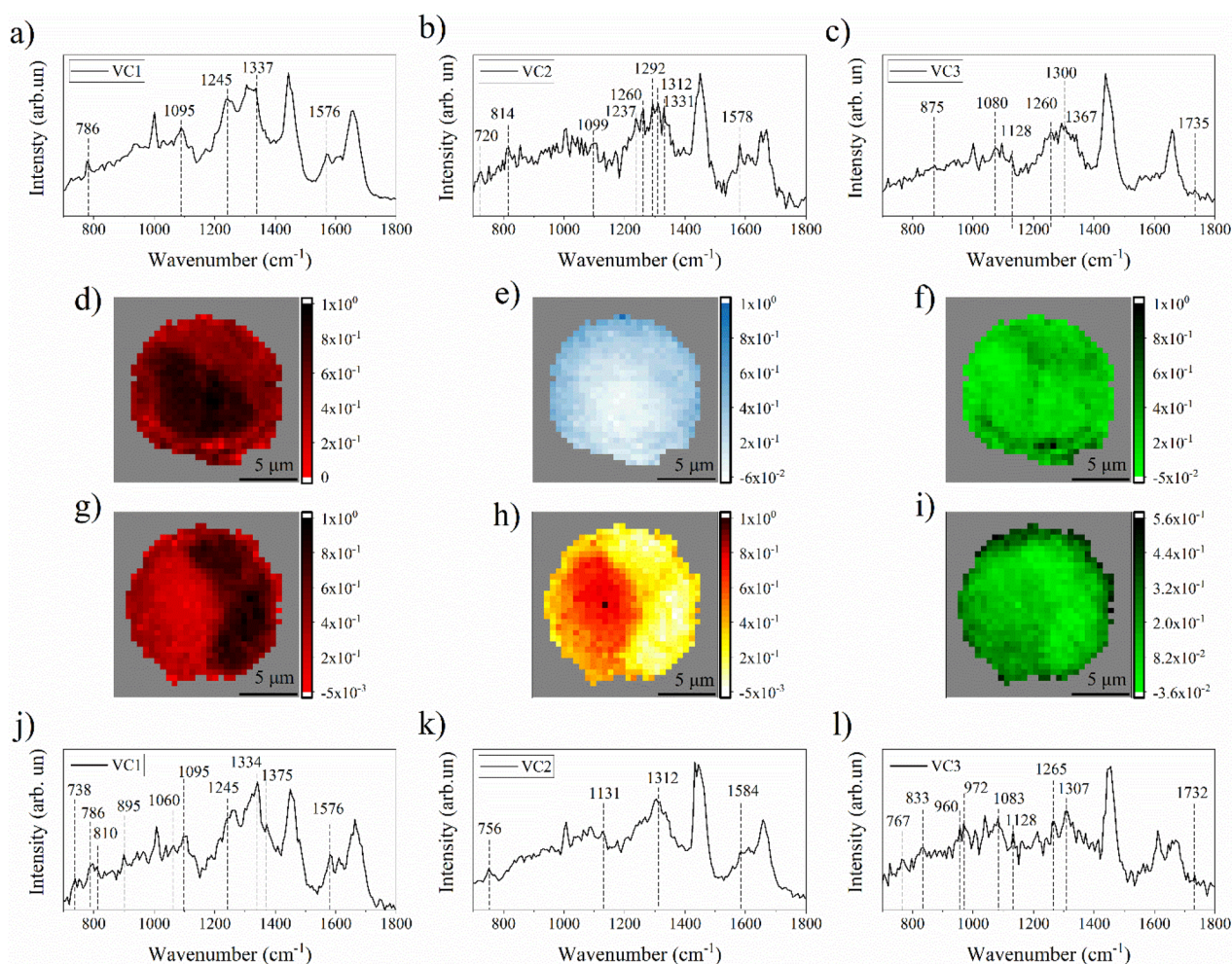

Figure 9. VCA-Raman imaging of control and CD-200 cells. a), b), c) VCA components of the control cell, used for imaging; d), e), f) corresponding images of the control cell. j), k), l) VCA components of the treated cell, used for imaging; g), h), i) corresponding images of the treated cell. Red is used for imaging based on nuclear acid component, green for lipid component, blue for RNA and orange for cytochrome c component.

as in treated cell, presumably due to the fact that RNA content of control cell is represented by VC2. Also, since this analysis is performed on each cell separately, it should be more successful in distinguishing intracellular spectral differences. On the contrary, described PCA-Raman imaging (Figure 8) captured both intracellular and intercellular differences, but their intensity range is mutually dependent: if the differences between cells are greater than the differences within cells, the image contrast of some cells may be insufficiently pronounced. Contrary to expected, in VC2 component, protein Raman markers were not distinctly distinguished. Instead of that, VC2 component of the control cell bears Raman markers which could be assigned to RNA. This component is slightly less intensively distributed in the nuclear than in cytoplasmic region. In the case of the treated cell, in VC2 component, peaks corresponding to resonance Raman markers of cytochrome c (marked with corresponding wavenumbers in Figure 9k) are distinguished. This component is pronounced in the cytoplasm and very weakly in the nuclear region of treated cell. Cytochrome c is pro-apoptotic factor, released from mitochondria to the cytoplasm in the early stages of apoptosis, whereas nuclear accumulation of cytochrome c starts later (Nur et al. 2004). The images obtained by VC3 are characterized by lower contrast, hence the differences between different compartments of the cells are hardly noticeable. In addition, the VC3 component differs between control and treated cells - it probably describes a presence of different set of lipids, combined with other classes of molecules. Similarly, in dominantly lipid VC components obtained from the analysis of other four cells (Figure S7, Supplementary material), the influence of different cellular molecules is visible. Extensive imaging of a large number of control and treated cells would be required to clarify which types of molecules are involved and to what extent each component is useful in describing the NP-induced state of the cell. With the current instrumentation, there are severe limitations for imaging large number of cells.

To summarize, standard biological tests showed the cytotoxic effect of CD NPs on MRC-5 cells starting from a dose of 200 μg/ml, which is accompanied by differences in Raman spectra, both between control and treated cells, and also between cells treated with different doses of NPs. The common general changes are an increase in the intensity of lipid modes and a decrease in the intensity of nucleic acid modes, detected by nnPCA. However, Raman modes that make the difference between the treated and the control cells are not the same for the two doses of NPs, indicating changes in different members of the lipid or nucleic acids class. Cells treated with a lower dose of NPs (200 μg/ml) are characterized by a marked increase in unsaturated fatty acids and phospholipid markers, especially phosphatidylserine, a marker of early apoptosis. After treatment with a high dose of NPs (400 μg/ml), cells with an increased intensity of lipid modes, but without phosphatidylserine markers can be clearly distinguished. At the same time, these cells are the ones in which there is no decrease in the content of nucleic acids in general, but only a decrease in the intensity of the RNA markers. The k-means clustering confirmed that these cells stand out as a distinct group, most likely as a group of autophagic cells characterized by a specific effect of CD NPs on them. It was proposed that most of the other CD-400 treated cells analyzed by Raman spectroscopy have undergone late apoptosis or necrosis. Raman images created based on score values for PCA components illustrated higher lipid content and reduced nuclear acids' area in CD-200 cells. Furthermore, Raman images based on VCA components abundance indicated that the amount of nucleic acids in the cytoplasm rather than in the nucleus is what distinguishes treated from untreated cells. Additionally, with the Raman-VCA method, it was possible to obtain an image of the treated cell based on the intensity of the Raman modes of cytochrome c, which indicated the presence of this apoptotic marker in the cytoplasm of the treated cell.

4. Conclusion

This study, based on multivariate single-cell Raman spectroscopy complemented by standard cytotoxicity assays and flow cytometry, unequivocally indicates the toxic effect of CD NPs on MRC-5 lung fibroblasts in culture, starting from the concentration of 200 μg/ml NPs. An early indicator of CD NPs' cytotoxicity is the deprivation of mitochondrial activity, which leads to cell death in a certain proportion of MRC-5 cells. Depending on the NPs dose, early or late apoptosis/necrosis is registered and related changes in biochemical composition are described. The most pronounced are the quantitative and qualitative changes in cellular lipid and nucleic acid content, which differentiate the NP-treated cells from the untreated ones, but also the cells treated with different doses of NPs from each other. Nevertheless, the other modality of cell

death, possibly autophagy, caused by interaction with NPs in dose higher than 200 μg/ml, is also indicated. Considering the small dimensions of the NPs and the hydrodynamic stability provided by the dextran coating, cytotoxic effect of CD NPs could have been expected. The absence of formation of CeO_2 NPs agglomerates, otherwise problematic in studies of their cytotoxicity, makes the results of this study particularly reliable.

The obtained results confirmed the usefulness of phospholipid-related Raman modes in assessing the effects of NPs and especially the importance of the Raman intensity ratio I_{1267}/I_{1300} as a parameter for assessing the degree of cell damage or the phase of cell death. In addition, it was demonstrated that the intensities of nucleic acids Raman markers vary with the degree of cell damage and can be associated with changes in RNA composition, hence used also for evaluating the effects of NPs. In a cell, RNA is difficult to distinguish from DNA by Raman spectra; therefore the insight provided by this study is significant. Moreover, integrating the PCA and VCA methods into Raman imaging, we were able to depict changes in the spatial distribution of RNA, but also the spatial arrangements of lipids, DNA and cytochrome c in treated cells through a single experiment. Finally, yet importantly, with the single-cell approach enabled by Raman spectroscopy, we were able to separate cell populations with different types of NP-induced biochemical changes and subsequently cross-analyze them using several parameters and statistical methods. In this way, we detected individual cells that underwent a specific effect of CD NPs, not registered by applied standard biological methods. Combining different, both standard and unconventional methods for Raman spectra analysis reveals the wealth of information about cell-NP interactions accessible by Raman spectroscopy.

Disclosure statement

No potential competing interest was reported by the authors.

Funding

Data availability statement

The data that support the findings of this study are available from the corresponding author, MM, upon reasonable request.

References

Abdi Goushbolagh, N., B. Farhood, A. Astani, A. Nikfarjam, M. Kalantari, and M. H. Zare. 2018. "Quantitative Cytotoxicity, Cellular Uptake and Radioprotection Effect of Cerium Oxide Nanoparticles in MRC-5 Normal Cells and MCF-7 Cancerous Cells." *BioNanoScience* 8 (3): 769–777. https://doi.org/10.1007/s12668-018-0538-z.

Ahlinder, L., B. Ekstrand-Hammarström, P. Geladi, and L. Osterlund. 2013. "Large Uptake of Titania and Iron Oxide Nanoparticles in the Nucleus of Lung Epithelial Cells as Measured by Raman Imaging and Multivariate Classification." *Biophysical Journal* 105 (2): 310–319. https://doi.org/10.1016/j.bpj.2013.06.017.

Alghamdi, A. A. A. 2023. "Biogenic Mg Doped CeO2 Nanoparticles via Hibiscus Sabdariffa and Its Potential Biological Applications." *Journal of Umm Al-Qura University for Applied Sciences* 9 (2): 132–141. https://doi.org/10.1007/s43994-023-00030-z.

Annangi, B., Z. Lu, J. Bruniaux, A. Ridoux, V. M. da Silva, D. Vantelon, J. Boczkowski, and S. Lanone. 2021. "Macrophage Autophagy Protects Mice from Cerium Oxide Nanoparticle-Induced Lung Fibrosis." *Particle and Fibre Toxicology* 18 (1): 6. https://doi.org/10.1186/s12989-021-00398-y.

ATCC. n.d. "CCL-171 MRC-5," ATCC (American Type Culture Collection) https://www.atcc.org/products/ccl-171.

Beleites, C., and V. Sergo. 2024. "hyperSpec: A Package to Handle Hyperspectral Data Sets in R," 0.100.0.

Brauchle, E., S. Thude, S. Y. Brucker, and K. Schenke-Layland. 2014. "Cell Death Stages in Single Apoptotic and Necrotic Cells Monitored by Raman Microspectroscopy." *Scientific Reports* 4 (1): 4698. https://doi.org/10.1038/srep04698.

Campbell, C. T., and C. H. F. Peden. 2005. "Oxygen Vacancies and Catalysis on Ceria Surfaces." *Science (New York, N.Y.)* 309 (5735): 713–714. https://doi.org/10.1126/science.1113955.

Chen, J., S. Patil, S. Seal, and J. F. McGinnis. 2006. "Rare Earth Nanoparticles Prevent Retinal Degeneration Induced by Intracellular Peroxides." *Nature Nanotechnology* 1 (2): 142–150. https://doi.org/10.1038/nnano.2006.91.

Chernenko, T., C. Matthäus, L. Milane, L. Quintero, M. Amiji, and M. Diem. 2009. "Label-Free Raman Spectral Imaging

of Intracellular Delivery and Degradation of Polymeric Nanoparticle Systems." *ACS Nano* 3 (11): 3552–3559. https://doi.org/10.1021/nn9010973.

Chernenko, T., L. Milane, C. Matthäus, M. Diem, and M. Amiji. 2013. "Raman Microspectral Imaging for Label-Free Detection of Nanoparticle-Mediated Cellular and Subcellular Drug Delivery." In *Drug Delivery Applications of Noninvasive Imaging*, pp. 70–90. John Wiley & Sons, Inc., Hoboken, New Jersey.

Corfe, B. M., C. Dive, and D. R. Garrod. 2000. "Changes in Intercellular Junctions during Apoptosis Precede Nuclear Condensation or Phosphatidylserine Exposure on the Cell Surface." *Cell Death and Differentiation* 7 (2): 234–235. https://doi.org/10.1038/sj.cdd.4400634.

Crow, P., B. Barrass, C. Kendall, M. Hart-Prieto, M. Wright, R. Persad, and N. Stone. 2005. "The Use of Raman Spectroscopy to Differentiate between Different Prostatic Adenocarcinoma Cell Lines." *British Journal of Cancer* 92 (12): 2166–2170. https://doi.org/10.1038/sj.bjc.6602638.

Cytion. n.d. "MRC-5 Cell Line: Human Fetal Lung Fibroblasts in Viral Research," Cytion. https://www.cytion.com/.

Czamara, K., K. Majzner, M. Z. Pacia, K. Kochan, A. Kaczor, and M. Baranska. 2015. "Raman Spectroscopy of Lipids: A Review." *Journal of Raman Spectroscopy* 46 (1): 4–20. https://doi.org/10.1002/jrs.4607.

Drasler, B., P. Sayre, K. G. Steinhäuser, A. Petri-Fink, and B. Rothen-Rutishauser. 2017. "In Vitro Approaches to Assess the Hazard of Nanomaterials." *NanoImpact* 8: 99–116. https://doi.org/10.1016/j.impact.2017.08.002.

Fazio, E., B. Gökce, A. De Giacomo, M. Meneghetti, G. Compagnini, M. Tommasini, F. Waag, et al. 2020. "Nanoparticles Engineering by Pulsed Laser Ablation in Liquids: Concepts and Applications." *Nanomaterials (Basel, Switzerland)* 10 (11): 2317. https://doi.org/10.3390/nano10112317.

Feng, N., Y. Liu, X. Dai, Y. Wang, Q. Guo, and Q. Li. 2022. "Advanced Applications of Cerium Oxide Based Nanozymes in Cancer." *RSC Advances* 12 (3): 1486–1493. https://doi.org/10.1039/d1ra05407d.

Ferraro, J. R., K. Nakamoto, and C. W. Brown. 2003. "Chapter 1 - Basic Theory." in: *Introductory Raman Spectroscopy*, 2nd ed., eds. J.R. Ferraro, K. Nakamoto, C.W. Brown, pp. 1–94. Academic Press, San Diego.

Guo, C., S. Robertson, R. J. M. Weber, A. Buckley, J. Warren, A. Hodgson, J. Z. Rappoport, et al. 2019. "Pulmonary Toxicity of Inhaled Nano-Sized Cerium Oxide Aerosols in Sprague–Dawley Rats." *Nanotoxicology* 13 (6): 733–750. https://doi.org/10.1080/17435390.2018.1554751.

Harvanova, M. P., J. Jiravova, J. Malohlava, K. B. Tomankova, D. Jirova, and H. Kolarova. 2017. "Raman Imaging of Cellular Uptake and Studies of Silver Nanoparticles Effect in BJ Human Fibroblasts Cell Lines." *International Journal of Pharmaceutics* 528 (1-2): 280–286. https://doi.org/10.1016/j.ijpharm.2017.05.076.

Hedegaard, M., C. Matthäus, S. Hassing, C. Krafft, M. Diem, and J. Popp. 2011. "Spectral Unmixing and Clustering Algorithms for Assessment of Single Cells by Raman Microscopic Imaging." *Theoretical Chemistry Accounts* 130 (4-6): 1249–1260. https://doi.org/10.1007/s00214-011-0957-1.

Hill, C., J. Li, D. Liu, F. Conforti, C. J. Brereton, L. Yao, Y. Zhou, et al. 2019. "Autophagy Inhibition-Mediated Epithelial–Mesenchymal Transition Augments Local Myofibroblast Differentiation in Pulmonary Fibrosis." *Cell Death & Disease* 10 (8): 591. https://doi.org/10.1038/s41419-019-1820-x.

Hussain, S., F. Al-Nsour, A. B. Rice, J. Marshburn, B. Yingling, Z. Ji, J. I. Zink, N. J. Walker, and S. Garantziotis. 2012. "Cerium Dioxide Nanoparticles Induce Apoptosis and Autophagy in Human Peripheral Blood Monocytes." *ACS Nano* 6 (7): 5820–5829. https://doi.org/10.1021/nn302235u.

Itzhak, D. N., S. Tyanova, J. Cox, and G. H. H. Borner. 2016. "Global, Quantitative and Dynamic Mapping of Protein Subcellular Localization." *eLife* 5: e16950. https://doi.org/10.7554/eLife.16950.

Jacobs, J. P., C. M. Jones, and J. P. Baille. 1970. "Characteristics of a Human Diploid Cell Designated MRC-5." *Nature* 227 (5254): 168–170. https://doi.org/10.1038/227168a0.4316953

Jana, S. K., P. Banerjee, S. Das, S. Seal, and K. Chaudhury. 2014. "Redox-Active Nanoceria Depolarize Mitochondrial Membrane of Human Colon Cancer Cells." *Journal of Nanoparticle Research* 16 (6): 2441. https://doi.org/10.1007/s11051-014-2441-z.

Jung, H., D. B. Kittelson, and M. R. Zachariah. 2005. "The Influence of a Cerium Additive on Ultrafine Diesel Particle Emissions and Kinetics of Oxidation." *Combustion and Flame* 142 (3): 276–288. https://doi.org/10.1016/j.combustflame.2004.11.015.

Karakoti, A. S., S. V. N. T. Kuchibhatla, K. S. Babu, and S. Seal. 2007. "Direct Synthesis of Nanoceria in Aqueous Polyhydroxyl Solutions." *The Journal of Physical Chemistry C* 111 (46): 17232–17240. https://doi.org/10.1021/jp076164k.

Krafft, C., M. A. Diderhoshan, P. Recknagel, M. Miljkovic, M. Bauer, and J. Popp. 2011. "Crisp and Soft Multivariate Methods Visualize Individual Cell Nuclei in Raman Images of Liver Tissue Sections." *Vibrational Spectroscopy* 55 (1): 90–100. https://doi.org/10.1016/j.vibspec.2010.09.003.

Lasalvia, M., G. Perna, and V. Capozzi. 2019. "Biochemical Changes in Human Cells Exposed to Low Concentrations of Gold Nanoparticles Detected by Raman Microspectroscopy." *Sensors* 19 (10): 2418. https://doi.org/10.3390/s19102418.

Liu, Y.-J., M. Kyne, S. Wang, S. Wang, X.-Y. Yu, and C. Wang. 2022. "A User-Friendly Platform for Single-Cell Raman Spectroscopy Analysis." *Spectrochimica Acta Part A: Molecular and Biomolecular Spectroscopy* 282: 121686. https://doi.org/10.1016/j.saa.2022.121686.

Ma, Y., W. Gao, Z. Zhang, S. Zhang, Z. Tian, Y. Liu, J. C. Ho, and Y. Qu. 2018. "Regulating the Surface of Nanoceria and Its Applications in Heterogeneous Catalysis." *Surface Science Reports* 73 (1): 1–36. https://doi.org/10.1016/j.surfrep.2018.02.001.

Ma, J. Y., R. R. Mercer, M. Barger, D. Schwegler-Berry, J. Scabilloni, J. K. Ma, and V. Castranova. 2012. "Induction of Pulmonary Fibrosis by Cerium Oxide Nanoparticles." *Toxicology and Applied Pharmacology* 262 (3): 255–264. https://doi.org/10.1016/j.taap.2012.05.005.

Mangalaraja, R. V., S. Ananthakumar, A. Schachtsiek, M. López, C. P. Camurri, and R. E. Avila. 2010. "Synthesis and Mechanical Properties of Low Temperature Sintered, Sm3+ Doped Nanoceria Electrolyte Membranes for IT-SOFC Applications." *Materials Science and Engineering: A* 527 (16-17): 3645–3650. https://doi.org/10.1016/j.msea.2010.01.025.

Mariño, G., M. Niso-Santano, E. H. Baehrecke, and G. Kroemer. 2014. "Self-Consumption: The Interplay of Autophagy and Apoptosis." *Nature Reviews. Molecular Cell Biology* 15 (2): 81–94. https://doi.org/10.1038/nrm3735.

Mayer, K. 2024. "hyperSpec.utils: Utility Functions to Work with Objects of the hyperSpec Class," 0.0.0.9002.

Ma, C., L. Zhang, T. He, H. Cao, X. Ren, C. Ma, J. Yang, R. Huang, and G. Pan. 2021. "Single Cell Raman Spectroscopy to Identify Different Stages of Proliferating Human Hepatocytes for Cell Therapy." *Stem Cell Research & Therapy* 12 (1): 555. https://doi.org/10.1186/s13287-021-02619-9.

Mazur, A. I., J. L. Monahan, M. Miljković, N. Laver, M. Diem, and B. Bird. 2013. "Vibrational Spectroscopic Changes of B-Lymphocytes upon Activation." *Journal of Biophotonics* 6 (1): 101–109. https://doi.org/10.1002/jbio.201200136.

Miletić, M., S. Aškrabić, J. Rüger, B. Vasić, L. Korićanac, A. S. Mondol, J. Dellith, J. Popp, I. W. Schie, and Z. Dohčević-Mitrović. 2020. "Combined Raman and AFM Detection of Changes in HeLa Cervical Cancer Cells Induced by CeO2 Nanoparticles – Molecular and Morphological Perspectives." *The Analyst* 145 (11): 3983–3995. https://doi.org/10.1039/c9an02518a.

Miletić, M., A. Vilotić, L. Korićanac, J. Žakula, M. J. Krivokuća, Z. Dohčević-Mitrović, and S. Aškrabić. 2023. "Spectroscopic Signature of ZnO NP-Induced Cell Death Modalities Assessed by Non-Negative PCA." *Spectrochimica Acta. Part A, Molecular and Biomolecular Spectroscopy* 288: 122180. https://doi.org/10.1016/j.saa.2022.122180.

Milligan, K., X. Deng, P. Shreeves, R. Ali-Adeeb, Q. Matthews, A. Brolo, J. J. Lum, J. L. Andrews, and A. Jirasek. 2021. "Raman Spectroscopy and Group and Basis-Restricted Non Negative Matrix Factorisation Identifies Radiation Induced Metabolic Changes in Human Cancer Cells." *Scientific Reports* 11 (1): 3853. https://doi.org/10.1038/s41598-021-83343-5.

Mittal, S., and A. K. Pandey. 2014. "Cerium Oxide Nanoparticles Induced Toxicity in Human Lung Cells: role of ROS Mediated DNA Damage and Apoptosis." *Biomed Research International*. 2014: 1–14. https://doi.org/10.1155/2014/891934.

Monteiro-Riviere, N. A., A. O. Inman, and L. W. Zhang. 2009. "Limitations and Relative Utility of Screening Assays to Assess Engineered Nanoparticle Toxicity in a Human Cell Line." *Toxicology and Applied Pharmacology* 234 (2): 222–235. https://doi.org/10.1016/j.taap.2008.09.030.

Naha, P. C., J. C. Hsu, J. Kim, S. Shah, M. Bouché, S. Si-Mohamed, D. N. Rosario-Berrios, et al. 2020. "Dextran-Coated Cerium Oxide Nanoparticles: A Computed Tomography Contrast Agent for Imaging the Gastrointestinal Tract and Inflammatory Bowel Disease." *ACS Nano* 14 (8): 10187–10197. https://doi.org/10.1021/acsnano.0c03457.

Nascimento, J. M. P., and J. M. B. Dias. 2005. "Vertex Component Analysis: A Fast Algorithm to Unmix Hyperspectral Data." *IEEE Transactions on Geoscience and Remote Sensing* 43 (4): 898–910. https://doi.org/10.1109/TGRS.2005.844293.

Niu, J., K. Wang, and P. E. Kolattukudy. 2011. "Cerium Oxide Nanoparticles Inhibit Oxidative Stress and Nuclear Factor-κB Activation in H9c2 Cardiomyocytes Exposed to Cigarette Smoke Extract." *The Journal of Pharmacology and Experimental Therapeutics* 338 (1): 53–61. https://doi.org/10.1124/jpet.111.179978.

Nourmohammadi, E., H. Khoshdel-Sarkarizi, R. Nedaeinia, H. R. Sadeghnia, L. Hasanzadeh, M. Darroudi, and R. Kazemi Oskuee. 2019. "Evaluation of Anticancer Effects of Cerium Oxide Nanoparticles on Mouse Fibrosarcoma Cell Line." *Journal of Cellular Physiology* 234 (4): 4987–4996. https://doi.org/10.1002/jcp.27303.

Nur, E. K. A., S. R. Gross, Z. Pan, Z. Balklava, J. Ma, and L. F. Liu. 2004. "Nuclear Translocation of Cytochrome c during Apoptosis." *The Journal of Biological Chemistry* 279 (24): 24911–24914. https://doi.org/10.1074/jbc.C400051200.

Ortiz-Zapater, E., J. Signes-Costa, P. Montero, and I. Roger. 2022. "Lung Fibrosis and Fibrosis in the Lungs: Is It All about Myofibroblasts?" *Biomedicines* 10 (6): 1423. https://doi.org/10.3390/biomedicines10061423.

Park, E. J., J. Choi, Y. K. Park, and K. Park. 2008. "Oxidative Stress Induced by Cerium Oxide Nanoparticles in Cultured BEAS-2B Cells." *Toxicology* 245 (1-2): 90–100. https://doi.org/10.1016/j.tox.2007.12.022.

Pavillon, N., and N. I. Smith. 2023. "Non-Invasive Monitoring of T Cell Differentiation through Raman Spectroscopy." *Scientific Reports* 13 (1): 3129. https://doi.org/10.1038/s41598-023-29259-8.

Perez, J. M., A. Asati, S. Nath, and C. Kaittanis. 2008. "Synthesis of Biocompatible Dextran-Coated Nanoceria with pH-Dependent Antioxidant Properties." *Small (Weinheim an Der Bergstrasse, Germany)* 4 (5): 552–556. https://doi.org/10.1002/smll.200700824.

Pešić, M., A. Podolski-Renić, S. Stojković, B. Matović, D. Zmejkoski, V. Kojić, G. Bogdanović, et al. 2015. "Anti-Cancer Effects of Cerium Oxide Nanoparticles and Its Intracellular Redox Activity." *Chemico-Biological Interactions* 232: 85–93. https://doi.org/10.1016/j.cbi.2015.03.013.

Rangan, S., S. Kamal, S. O. Konorov, H. G. Schulze, M. W. Blades, R. F. B. Turner, and J. M. Piret. 2018. "Types of Cell Death and Apoptotic Stages in Chinese Hamster Ovary Cells Distinguished by Raman Spectroscopy." *Biotechnology and Bioengineering* 115 (2): 401–412. https://doi.org/10.1002/bit.26476.

Reed, K., A. Cormack, A. Kulkarni, M. Mayton, D. Sayle, F. Klaessig, and B. Stadler. 2014. "Exploring the Properties and Applications of Nanoceria: Is There Still Plenty of Room at the Bottom?" *Environmental Science: Nano* 1 (5): 390–405. https://doi.org/10.1039/C4EN00079J.

Samuel, A. Z., K. Sugiyama, M. Ando, and H. Takeyama. 2022. "Direct Imaging of Intracellular RNA, DNA, and Liquid–Liquid Phase Separated Membraneless Organelles with Raman Microspectroscopy." *Communications Biology* 5 (1): 1383. https://doi.org/10.1038/s42003-022-04342-4.

Schie, I. W., L. Alber, A. L. Gryshuk, and J. W. Chan. 2014. "Investigating Drug Induced Changes in Single, Living Lymphocytes Based on Raman Micro-Spectroscopy." *The Analyst* 139 (11): 2726–2733. https://doi.org/10.1039/c4an00250d.

Shin, H. J., J. H. Lee, Y. D. Kim, I. Shin, T. Sim, and D.-K. Lim. 2019. "Raman-Based in Situ Monitoring of Changes in Molecular Signatures during Mitochondrially Mediated Apoptosis." *ACS Omega* 4 (5): 8188–8195. https://doi.org/10.1021/acsomega.9b00629.

Short, K. W., S. Carpenter, J. P. Freyer, and J. R. Mourant. 2005. "Raman Spectroscopy Detects Biochemical Changes Due to Proliferation in Mammalian Cell Cultures." *Biophysical Journal* 88 (6): 4274–4288. https://doi.org/10.1529/biophysj.103.038604.

Sigg, C. 2018. "nsprcomp: Non-Negative and Sparse PCA." https://cran.r-project.org/web/packages/nsprcomp/index.html.

Spezzati, G., K. Fant, A. Ahniyaz, M. Lundin-Johnson, E. J. M. Hensen, H. Langermans, and J. P. Hofmann. 2017. "Synthesis, Physicochemical Characterization, and Cytotoxicity Assessment of CeO2 Nanoparticles with Different Morphologies." *European Journal of Inorganic Chemistry* 2017 (25): 3184–3190. https://doi.org/10.1002/ejic.201700248.

Srinivas, A., P. J. Rao, G. Selvam, P. B. Murthy, and P. N. Reddy. 2011. "Acute Inhalation Toxicity of Cerium Oxide Nanoparticles in Rats." *Toxicology Letters* 205 (2): 105–115. https://doi.org/10.1016/j.toxlet.2011.05.1027.

Tolstik, E., L. A. Osminkina, C. Matthäus, M. Burkhardt, K. E. Tsurikov, U. A. Natashina, V. Y. Timoshenko, R. Heintzmann, J. Popp, and V. Sivakov. 2016. "Studies of Silicon Nanoparticles Uptake and Biodegradation in Cancer Cells by Raman Spectroscopy." *Nanomedicine: nanotechnology, Biology, and Medicine* 12 (7): 1931–1940. https://doi.org/10.1016/j.nano.2016.04.004.

Walkey, C., S. Das, S. Seal, J. Erlichman, K. Heckman, L. Ghibelli, E. Traversa, J. F. McGinnis, and W. T. Self. 2015. "Catalytic Properties and Biomedical Applications of Cerium Oxide Nanoparticles." *Environmental Science. Nano* 2 (1): 33–53. https://doi.org/10.1039/C4EN00138A.

Wieland, K., M. Masri, J. von Poschinger, T. Brück, and C. Haisch. 2021. "Non-Invasive Raman Spectroscopy for Time-Resolved in-Line Lipidomics." *RSC Advances* 11 (46): 28565–28572. https://doi.org/10.1039/d1ra04254h.

Yazici, H., E. Alpaslan, and T. J. Webster. 2015. "The Role of Dextran Coatings on the Cytotoxicity Properties of Ceria Nanoparticles Toward Bone Cancer Cells." *JOM Journal of the Minerals Metals and Materials Society.* 67 (4): 804–810. https://doi.org/10.1007/s11837-015-1336-5.

Zhou, C., X. Xu, L. Dai, H. Gong, and S. Lin. 2021. "Chemical-Mechanical Polishing Performance of Core-Shell Structured Polystyrene@Ceria/Nanodiamond Ternary Abrasives on Sapphire Wafer." *Ceramics International* 47 (22): 31691–31701. https://doi.org/10.1016/j.ceramint.2021.08.048.

Zuser, E., T. Chernenko, J. Newmark, M. Miljković, and M. Diem. 2010. "Confocal Raman Microspectral Imaging (CRMI) of Murine Stem Cell Colonies." *The Analyst* 135 (12): 3030–3033. https://doi.org/10.1039/c0an00546k.